Three-Dimensional Analysis of Particle Distribution on Filter Layers inside N95 Respirators by Deep Learning

Hye Ryoung Lee, Lei Liao, Wang Xiao, Arturas Vailionis, Antonio J. Ricco, Robin White, Yoshio Nishi, Wah Chiu, Steven Chu, and Yi Cui*

Cite This: https://dx.doi.org/10.1021/acs.nanolett.0c04230
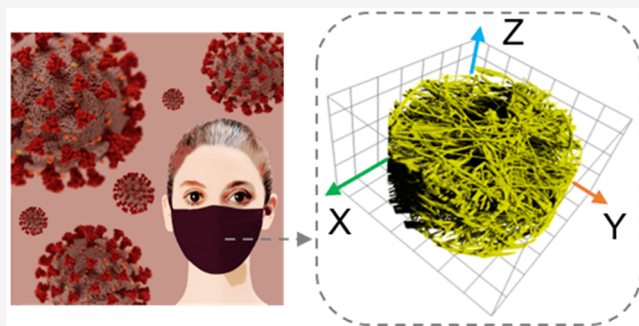
Read Online

ACCESS | Metrics & More | Article Recommendations | Supporting Information

ABSTRACT: The global COVID-19 pandemic has changed many aspects of daily lives. Wearing personal protective equipment, especially respirators (face masks), has become common for both the public and medical professionals, proving to be effective in preventing spread of the virus. Nevertheless, a detailed understanding of respirator filtration-layer internal structures and their physical configurations is lacking. Here, we report three-dimensional (3D) internal analysis of N95 filtration layers via X-ray tomography. Using deep learning methods, we uncover how the distribution and diameters of fibers within these layers directly affect contaminant particle filtration. The average porosity of the filter layers is found to be 89.1%. Contaminants are more efficiently captured by denser fiber regions, with fibers <1.8 μm in diameter being particularly effective, presumably because of the stronger electric field gradient on smaller diameter fibers. This study provides critical information for further development of N95-type respirators that combine high efficiency with good breathability.

KEYWORDS: *COVID-19, N95 respirator, particle distribution, face mask, deep learning, X-ray tomography*

The zoonotic severe acute respiratory syndrome coronavirus 2 (SARS-CoV-2) that causes COVID-19 has led to a global pandemic, raising significant societal challenges worldwide in healthcare, economics, education, and governance, all as wealth disparities worsen. Many countries have adopted moderate to drastic measures to prevent rapid spread of the virus by mandating periods of quarantine, social distancing, wearing of respirators, and recommending improved general hygiene including frequent hand washing. Despite such efforts, thousands of new cases are diagnosed worldwide each day, with rapid increases recorded whenever lockdown orders are eased and schools and face-to-face businesses reopen.

Human coronavirus (HCoV) infection can cause respiratory diseases, with two major outbreaks in the recent past: severe acute respiratory syndrome coronavirus (SARS-CoV) and Middle East respiratory syndrome coronavirus (MERS-CoV).[1] SARS-CoV-2 has similarities to the other HCoVs in size, structure, and chemical properties, yet significant portions of this virus along with COVID-19 disease itself are poorly understood, including critical details of transmission range, periods of contagiousness, and mechanisms of infection.[2,3] As new symptoms and post-recovery conditions evolve, the Centers for Disease Control and Prevention (CDC) and the World Health Organization (WHO) have updated symptom lists to inform the public. In this dynamic and urgent situation, the combined academic, government, and commercial science community has focused major research effort on uncovering essential details of SARS-CoV-2 and COVID-19 in addition to seeking vaccines and improved medical treatments.

Studies show that virus-containing aerosols can linger in the air for many hours and travel more than 6 to 8 m.[4-6] Thus, as the pandemic developed, the importance of personal protective equipment (PPE) increased, fueling worldwide demand for N95 respirators, which filter out at least 95% of particles around 0.3 μm in diameter (particle size with maximum filter penetration, i.e., the transition from impaction-based capture to diffusion-based capture). Equivalents of the United States N95 designation include FFP2, P2, PFF2, KF94, KN95, and DS/DL2 in the European Union, Australia/New Zealand, Brazil, South Korea, China, and Japan, respectively; all filter at least 94% or 95% of particles. Given the short supply of N95 respirators, disinfection methods for mask reuse as well as alternative mask types have been actively studied.[7-10] Most countries mandate the wearing of respirators in public spaces.

A

Protection of first responders and medical professionals is understandably emphasized, as is, to varying degrees, safeguarding teachers and workers with high risk from repeated or prolonged exposure to large numbers of people.

The efficacy of N95 respirators is usually measured by overall filtration efficiency for a defined incident flow of particles carried by a stream of air forced through the filtration layers while the pressure differentials are measured. Nonetheless, neither the internal structures of these layers nor the particle penetration and capture mechanisms have been well studied. In this study, we used X-ray microscopy (XRM) to nondestructively visualize, analyze, and understand the three-dimensional internal configurations and adhesion of particles to polymer fibers inside N95 respirators. Such analysis is critical to assess the effectiveness of these respirators, which were not originally studied and designed for protection from HCoV viruses, including SARS-CoV-2. Artificial intelligence (A.I.), specifically deep learning (DL), was used to segment and analyze 3D data sets obtained by XRM to efficiently evaluate the large volume of data, consisting of over a thousand slices for each sample. We investigated key physical features of N95 respirators, quantifying large data sets for porosity, fiber distribution, and particle distribution in multiple samples prepared by varying quantities of particle deposition.

Wearing respirators is one of the most effective ways to protect people from pathogen-related diseases including COVID-19. Typical commercial respirators consist of multiple layers to accommodate both good filtration efficiency and reasonable breathability, as shown in Figure 1a (SARS-CoV-2 image: by courtesy of the CDC/Alissa Eckert, MSMI, and Dan Higgins, MAMS). The meltblown filter fabric in such

respirators, the key component for providing high filtration efficiency, is usually made of polypropylene polymer fibers, which are shown in the SEM of Figure 1b.

We measured the 3D structure of the meltblown polypropylene filter fabric layer of N95 respirators by XRM (Carl Zeiss X-ray Microscopy Inc., Xradia Versa 520 and 810 Microscopes). A functional schematic of XRM is shown in Figure 1c. XRM nondestructively images a wide range of materials with varying degrees of densities, including "soft materials," such as polymers, which are typically damaged by electron-beam irradiation during acquisition of scanning-electron micrographs; therefore, the materials often require additional sample processing such as surface coatings or must be imaged using a low-temperature process. In contrast, XRM, in particular, X-ray computed tomography (XCT), provides detailed geometrical and relative density information from a volume measurement of the samples without damaging or altering the internal structures. Multiple projection images are the basis of 3D structural images reconstructed after drift correction.

Unlike medical CT, materials-research-based XCT generally acquires data as the sample stage rotates as shown in Figure 1c. We used two XRM systems: the Xradia 520 (micro-XRM or micro-CT) offers a relatively large field of view with pixel size of 0.5−0.7 μm; the Xradia a 810 (nano-XRM or nano-CT) provides high-resolution imaging with spatial resolution down to 50 nm, similar to synchrotron X-ray spatial resolution. Figure 1d is an exemplary 3D image of an N95 filter layer measured by Xradia 520 and then reconstructed by XMReconstructor (Carl Zeiss X-ray Microscopy Inc.). Reconstructed X-ray images were processed by deep learning algorithms as summarized by Figure 1e.

Deep learning (DL), a technique inspired by the human nervous system and structurally mimicking the human brain,[11] was used in this study to identify features in the tomography images obtained from XRM. DL is a subset of machine learning, which is a subfield of artificial intelligence (Figure S1a). DL is particularly important when traditional machine learning fails to scale in "big data" applications (Figure S1b); therefore, it is utilized in many everyday applications including Google Translate, photo sorting in smart phones, medical imaging, self-driving cars, and face and speech recognition.[11,12] We exploit DL's demonstrated image-recognition efficacy by implementing it via U-net convolutional neural networks for the structural analysis of N95 filter fabric. U-net convolutional neural networks are one of the popular DL architectures for image processing. Originally developed for bioimaging applications, the U-net network is a very efficient image-segmentation method that requires very few training images.[13−15] Image segmentation is the process of assigning image data components to sets of groups, also called classes, that have common properties.[16] U-net architecture has proven to be very appropriate for our 3D X-ray image segmentation: each pixel can be separately classified rather than assigning the entire output to a single class.

DL is particularly helpful to resolve adjacent features from materials with low Z-contrast (similar atomic number): relative to carbon and oxygen that comprise the polymer fibers, the contaminating NaCl particles used in this study have only moderate Z-contrast. Quantitative analysis of the sample was especially challenging as many particles are near or less than the resolution limit of the XRM. With DL training, the models
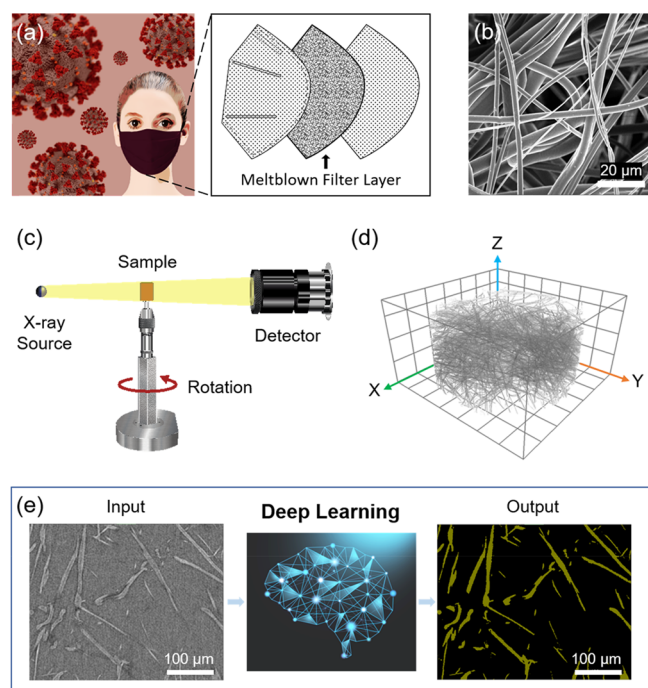

Figure 1. (a) Schematic images of wearing a respirator against SARS-CoV-2 and multilayer of N95 respirators, (b) an SEM image of N95 filter fabric layer, (c) a simplified illustration of the X-ray microscope (XRM), (d) an example of a 3D X-ray image of N95 filter fabric layer obtained by XRM, and (e) data process flow of 3D X-ray data sets analyzed by deep learning techniques with input/output image examples.
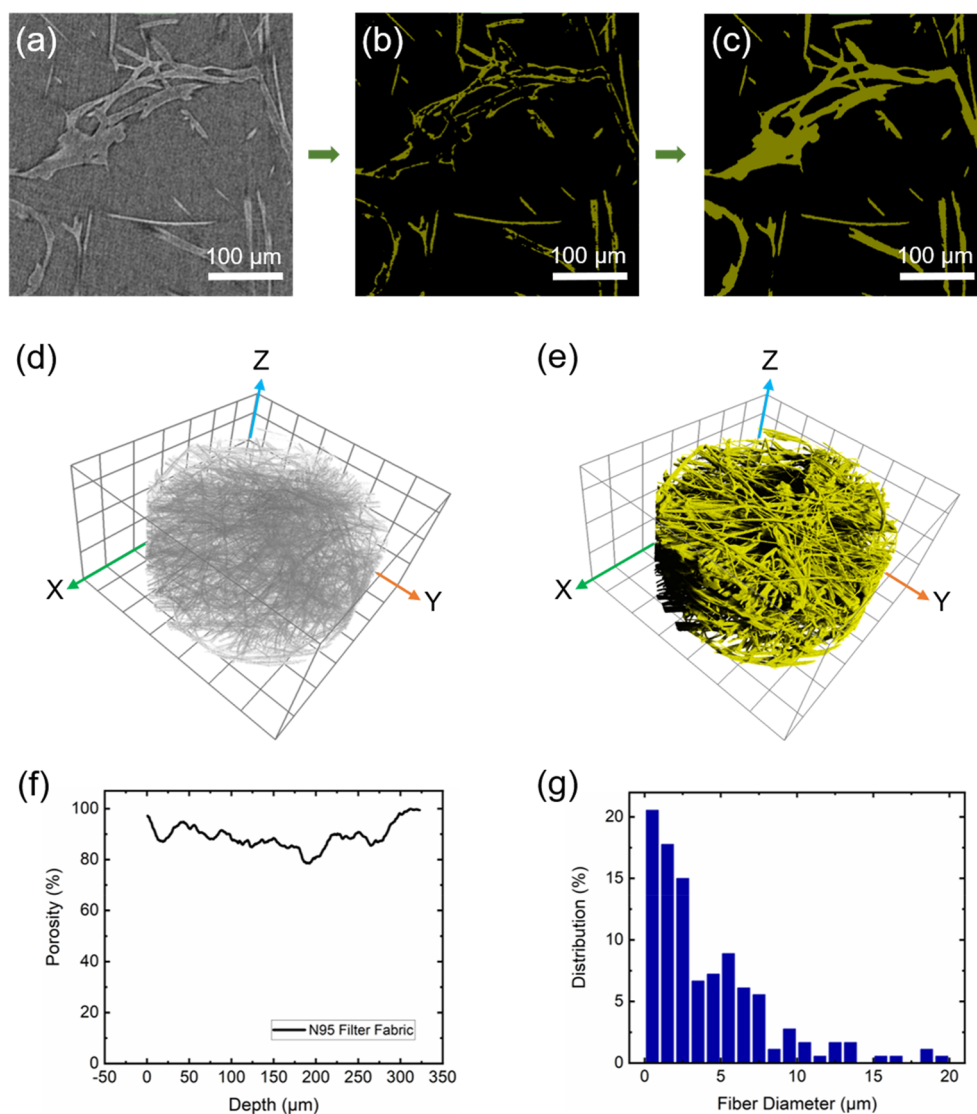
Figure 2. (a) Reconstructed XRM image of N95 filter fabric layer. (b,c) Deep-learning-assisted image segmention of X-ray slices captured from 3D XCT images; the yellow color indicates segmented polymer fibers and the black background is empty space. (d,e) 3D perspective views of the filter fabric layer; the gray image on the left is the reconstructed 3D X-ray tomographic image, and the yellow one on the right is a segmented 3D image from deep learning models. Each grid box is 100 μm × 100 μm in size. (f) Porosity of single N95 meltblown filter fabric as a function of depth into the layer. (g) Statistical distributions of fiber diameters of meltblown polypropylene fibers within filters of N95 respirators measured from SEM.

distinguished key features and, with repeated training, enabled extraction of quantitative details from large data sets.

Initially, reconstructed X-ray tomographic images were processed by several deep-learning models, with U-Net architecture being ultimately selected because it provides the best feature recognition for our data sets. Training data were collected through manual segmentation in representative local areas at various locations throughout the data set. Training was continued iteratively using an Adadelta optimization algorithm, while monitoring model performance. Up to the point at which the model showed good agreement with the original data sets, iterative training and model modification continued. After training, all segmented image slices were visually inspected before quantitative analysis was performed.

Figure 2a shows the reconstructed image, while Figure 2b,c shows the DL-processed 2D images obtained from 3D X-ray tomography. As training continues, the DL model recognizes the fiber features more accurately. Figure 2d,e and Figure S2a–d display 3D X-ray images of the filter fabric layers from

various viewing angles. The left (gray) results are reconstructed X-ray images and the right (yellow) ones are DL-segmented images. A 3D video of DL-processed propylene filter layer is in Movie 1.

N95 respirators consist of multiple layers to optimize filtration efficiency and breathability; the key filtration layer usually has meltblown polypropylene fibers that are low cost, chemically robust, and readily scaled to high-volume manufacturing.[17−19] The typical meltblown layer thickness used in commercially available N95 respirators is about 200− 400 μm. The average layer thickness studied here is 345 μm with porosity of the meltblown fabric of 78.5−99.8% as shown in Figure 2f. Though most manufacturers use two or more layers of meltblown filter fabric inside N95 respirators, we studied a single layer of the filter fabric to analyze one layer's characteristics and understand the filtration mechanism. The fibers, characterized by SEM and XRM, were found to be randomly distributed in the meltblown filter fabric, as shown in Figure 1b,d and Figure 2d,e. A randomized network is
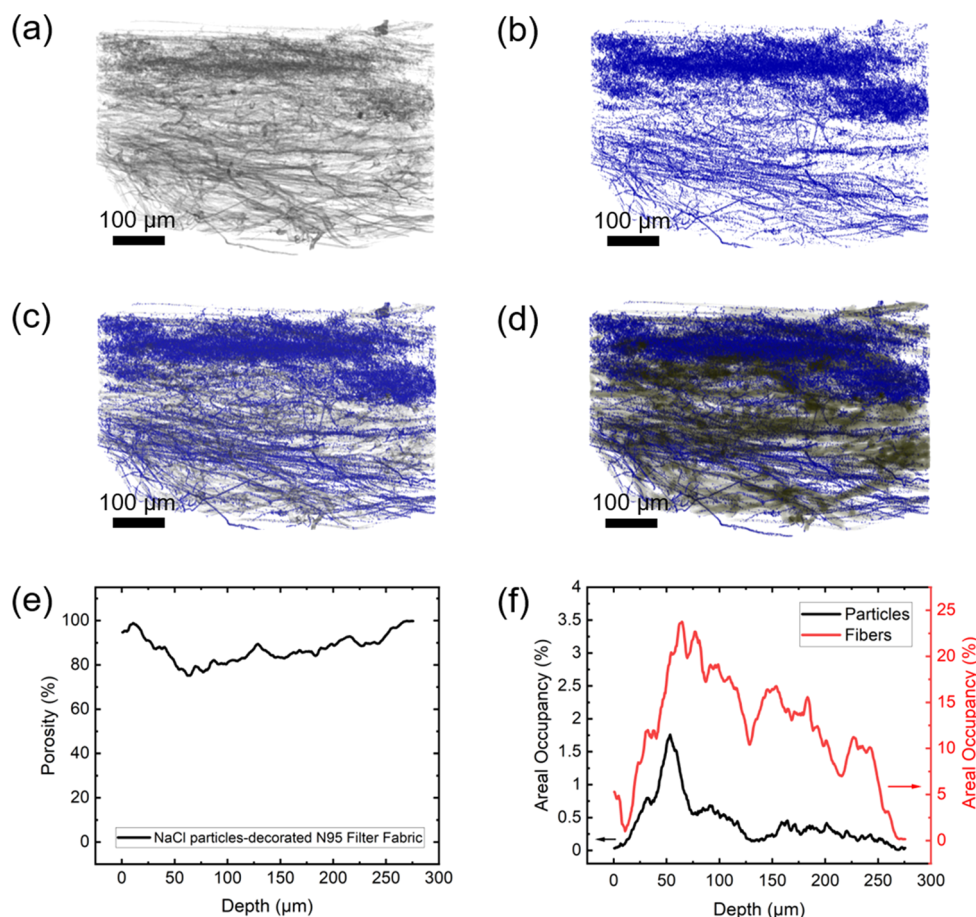
Figure 3. Images of NaCl particle-decorated meltblown filter fabric: (a) reconstructed X-ray tomographic volume, (b) deep-learning-assisted segmented particles only, (c) deep-learning-assisted segmented particles overlaid on reconstructed X-ray tomographic image, and (d) deep-learning-assisted segmented particles on deep-learning-assisted segmented fabric fibers; blue color in (b), (c), and (d) indicates NaCl particles. (e) Porosity of the filter fabric and (f) areal occupancies of fibers and NaCl particles vs depth into the meltblown layer. NaCl mass loading was 1.02 mg/cm^2.

favorable for effective filtration compared with aligned or regular structures that could include facile channeling flow-through paths for droplets or aerosols. The distribution-weighted average fiber diameter measured from SEM images is 4.2 ± 3.9 μm, as seen in Figure 2g.

Sodium chloride (NaCl) particle-decorated N95 meltblown fabric was tested for filtration efficiency and internal contaminant capture morphology and mechanism; Figure 3a−d shows NaCl particle-decorated fabric morphology acquired by micro-XRM and the segmented results obtained by DL models. A 3D video of DL-processed NaCl particle-decorated polypropylene filter layer is in Movie 2. The count median diameter of NaCl particles used in this study is 75 ± 20 nm, which is similar to virus particle sizes. The mass loading of NaCl particles in the sample was 1.02 mg/cm^2. Not surprisingly, Figure 3 reveals that particles accumulate more on the outer surface, upon which they are first incident, than on the innermost surface, closest to the wearer's face. The overall porosity of the NaCl particle-decorated filter layer is reduced to the range of 75.2−99.8% (average: 87.3%) from its value prior to particle deposition of 78.5−99.8% (average: 89.1%). NaCl particle loading uniformity was also characterized as a function of depth into the filtration layer for three mass-loading conditions: 0.17, 0.51, and 1.02 mg/cm^2 (Figure S4(a-f)).

In addition to the loading-dependent concentration gradient of contaminants across the depth of the filter layer, the second factor that significantly affects contaminant particle concentration distribution is uniformity of fiber distribution. While the meltblown fabric has (pseudo-) random networks, there exists in-plane and out-of-plane nonuniformity throughout the depth, resulting in contaminant distribution variations as dense areas catch particles more efficiently. The red curves in Figure 3f and Figure S4b,d, f indicate the areal occupancy of the fibers as a function of depth into the fabric layer; the black curves indicate the particle areal densities. (An aerial occupancy of 100% corresponds to no voids between fibers or particles at a given depth into the filter; the total area analyzed was 100 cm^2 of fabric.) Figure 3f and Figure S4b,d,f show that the trend of the particle occupancy (black curves) follows that of the fiber density (red curves). In other words, more particles can be captured in denser fiber areas. Also, it is likely that nonuniformity may be caused by dendritic particle accumulation, i.e., particles "piling up" on those previously captured. In addition, particle buildup at a given depth is influenced by the preceding fiber density along the particles' paths, creating complex dynamics that may affect each particle's deposition location.

Filtration efficiency tests used the Automated Filter Tester 8130A (TSI, Inc.) with 85 L/min flow rate and NaCl solution
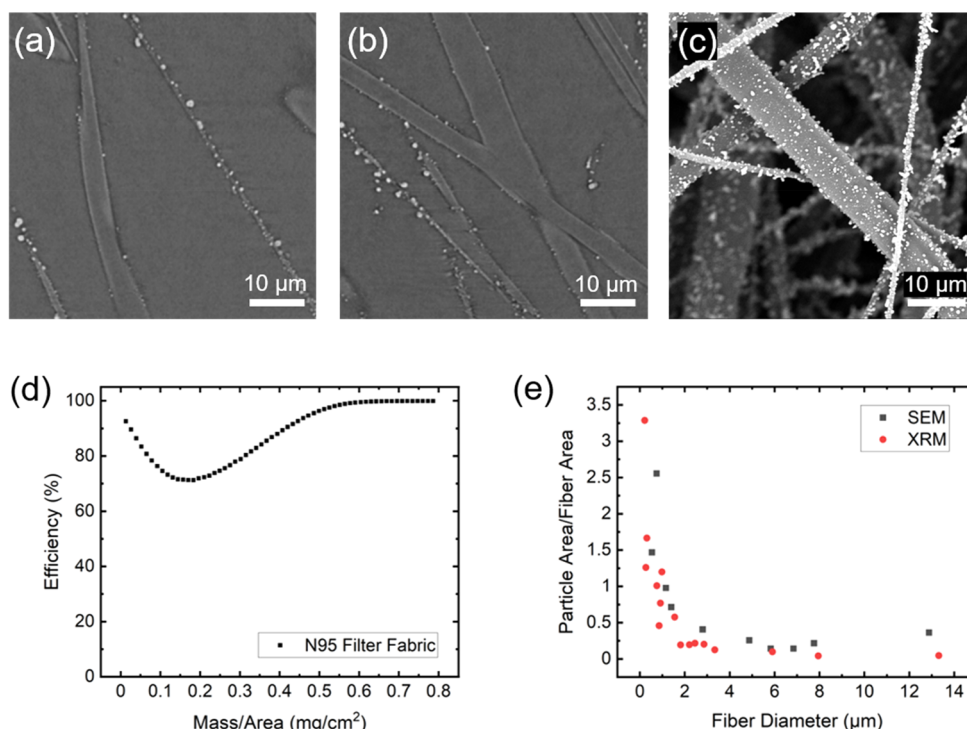
Figure 4. (a,b) High-resolution nano-XRM images of several fibers with NaCl particles adhered show more captured particles per unit length as fiber diameter decreases. (c) An SEM image of polypropylene meltblown fabric with adherent NaCl particles. (d) Filtration efficiency graph of the meltblown fabric as a function of the deposited mass density of NaCl particles. (e) Dependence of measured particle capture area per unit fiber area on fiber diameter.

(2 wt % in water) to generate aerosol particles. The experimental configuration leads to the complete evaporation of water from each aerosol droplet before it reaches the respirator, such that solid NaCl particles with 0.26 μm median diameter are incident on the material being tested. Each sample was cut to approximately 15 cm × 15 cm. This process, including use of NaCl particles, is the standard testing protocol for N95 respirators for certification and assessment by CDC's National Institute for Occupational Safety and Health (NIOSH). The loading-and-efficiency test was done using a single meltblown fabric filter layer, even though N95 respirators usually include two or more layers depending on the manufacturer and intended application(s). The additional layers are often made of different materials that provide moisture-repellency, preventing transmission of large droplets and aerosols.

Dependence of the particle capture efficiency on total particle loading was investigated to understand the efficiency changes during filtration. Figure 4d reveals that meltblown layer particle capture efficiency starts at close to the expected 92.6% but decreases to a minimum of ∼71.3% at ∼0.183 mg/cm^2 of loading; this may result from the decay or neutralization of electrostatic charge initially present on the filter layer. As NaCl particle loading proceeds further, capture efficiency increases, reaching ∼99.5% at loading of ∼0.60 mg/cm^2, likely because the accumulated particles start to block voids between fibers. While better filtration efficiency is desirable, blocking filter voids hampers air permeability, directly related to user breathability. The balance and trade-off of filtration efficiency and respirator breathability are critical for efficient respirator design while protecting the wearer's health.

The diameter distribution in the meltblown polypropylene layer in Figure 2g raises the question of which fiber size would

provide the greatest filtration effect. Interestingly, NaCl particles accumulate more on the thinnest fibers (observed consistently by both SEM and XRM). The XRM images of several isolated fibers in Figure 4a,b and SEM image in Figure 4c clearly demonstrate this phenomenon: DL-assisted analysis of 3D XRM tomographic images shows that the effect persists throughout the thickness of the filtration layer. Quantification of captured particle area per fiber area, Figure 4e, shows that fibers <1.8 μm in diameter are significantly more effective at particle capture than larger fibers. This may stem from the magnitude of the electric field gradient associated with the static charge, which is generated by the corona discharge process step, utilized by most manufacturers to increase particle capture efficiency. The better the capture efficiency, particularly if it is associated with small fiber diameters, the better breathability can be for a given overall filtration efficiency. Further aspects of the corona discharge mechanism are explained in previous studies; the mechanistic details of particle capture as a function of fiber type and diameter are under active investigation.[20−24]

In summary, we used X-ray microscopy to shed light on the 3D microstructure and morphology of N95 respirator filtration layers, and to understand the adhesion distribution of contaminant particles to polymer fibers. This analysis will aid evaluations of the efficacy of respirators against a variety of contaminants, including SARS-CoV-2. Deep-learning algorithms were proven to be essential to segment and analyze a large number of 3D tomography data sets through trained models. Fiber diameters, density distributions, and overall fabric porosity were characterized, as were particle distributions in various samples prepared with different amounts of particle deposition. We found that the fiber diameter plays a crucial role, with capture efficiency drastically improved for

fibers <1.8 μm in diameter, likely related to the electric field gradient. We also observed that fiber distribution directly affects contaminant-capture efficiency: dense fiber areas trap more particles. We conclude that appropriate design of fiber density gradients in combination with well-chosen fiber diameter distributions can, in future N95 respirators, lead to high particle-capture efficiencies without sacrificing good breathability over a larger total particle loading range relative to current filter characteristics.

METHODS

Sample Preparation. TM95 meltblown fabric (Guangdong Meltblown Technology Co. Ltd.) samples were used for filtration testing. Each sample was cut to approximately 15 cm × 15 cm.

SEM Analysis. Scanning electron microscope images were taken using a Phenom Pro SEM and Thermofisher Helios at 10 kV.

X-ray Microscope Analysis. Zeiss Xradia 520 and Zeiss Xradia Ultra 810 X-ray Microscopes (XRMs) (Carl Zeiss X-ray Microscopy Inc., Pleasanton, CA) were used to obtain X-ray tomographic images and ORS Dragonfly software (version 4.1 and 2020.1) and ImageJ[25] software were used for the data analysis. Deep Learning Module in Dragonfly software[26,27] was used for image segmentation via 15−20 slices for training each data set. Data augmentation of factor 10 with rotation, horizontal and vertical flipping, shearing (of 2 degrees) and scaling (0.9 to 1.1) was implemented to reduce the processing time. Dice loss and AdaDelta optimization method were used to train images.

Fiber and particle occupancy results were quantified by full-depth 3D filter fabric data collected using the Zeiss Xradia 520 system. Particle adhesion dependence on fiber diameter was confirmed by the data obtained from the Zeiss Xradia Ultra 810 system. Reconstruction was performed using commercial software package XMReconstructor (version 14.0.1, Carl Zeiss X-ray Microscopy Inc., Pleasanton, CA).

ASSOCIATED CONTENT

Ⓢ Supporting Information

The Supporting Information is available free of charge at https://pubs.acs.org/doi/10.1021/acs.nanolett.0c04230.

> The scope of deep learning, reconstructed and DL-processed 3D X-ray images, porosity and areal occupancy graphs (PDF)

Ⓦ Web-Enhanced Features

3D videos of DL-processed polypropylene filter layers with and without NaCl particles. High-resolution videos are available upon request.

AUTHOR INFORMATION

Corresponding Author

Yi Cui − *Stanford Institute for Materials and Energy Sciences, SLAC National Accelerator Laboratory, Menlo Park, California 94025, United States; Department of Materials Science and Engineering, Stanford University, Stanford, California 94305, United States;* ⓞ orcid.org/0000-0002-6103-6352; Email: yicui@stanford.edu

Authors

Hye Ryoung Lee − *Geballe Laboratory for Advanced Materials, Stanford University, Stanford, California 94305,*
United States; Stanford Institute for Materials and Energy Sciences, SLAC National Accelerator Laboratory, Menlo Park, California 94025, United States; ⓞ orcid.org/0000-0003-4546-4880

Lei Liao − *4C Air, Inc., Sunnyvale, California 94089, United States*

Wang Xiao − *4C Air, Inc., Sunnyvale, California 94089, United States*

Arturas Vailionis − *Stanford Nano Shared Facility, Stanford University, Stanford, California 94305, United States; Department of Physics, Kaunas University of Technology, LT-51368 Kaunas, Lithuania*

Antonio J. Ricco − *Department of Electrical Engineering, Stanford University, Stanford, California 94305, United States*

Robin White − *Carl Zeiss X-ray Microscopy, Inc., Pleasanton, California 94588, United States*

Yoshio Nishi − *Department of Electrical Engineering, Stanford University, Stanford, California 94305, United States*

Wah Chiu − *Department of Bioengineering, James H. Clark Center, Stanford University, Stanford, California 94305, United States; Division of CryoEM and Bioimaging, SSRL, SLAC National Accelerator Laboratory, Menlo Park, California 94025, United States;* ⓞ orcid.org/0000-0002-8910-3078

Steven Chu − *Department of Physics and Department of Molecular and Cellular Physiology, Stanford University, Stanford, California 94305, United States*

Complete contact information is available at:
https://pubs.acs.org/10.1021/acs.nanolett.0c04230

Author Contributions

H.R.L., L.L., and Y.C. designed the experiments. H.R.L., L.L., A.V., and R.W. collected the data. All authors analyzed the data, interpreted results, and wrote the manuscript.

Notes

The authors declare the following competing financial interest(s): Professors Steven Chu and Yi Cui are founders and shareholders of the company 4C Air, Inc. They are inventors on patent PCT/US2015/065608. Authors Lei Liao and Wang Xiao are employed by 4C Air, Inc.

ACKNOWLEDGMENTS

REFERENCES

(1) Fung, T. S.; Liu, D. X. Human Coronavirus : Host-Pathogen Interaction. *Annu. Rev. Microbiol.* **2019**, *73*, 529−560.

(2) Wu, F.; Zhao, S.; Yu, B.; Chen, Y. M.; Wang, W.; Song, Z. G.; Hu, Y.; Tao, Z. W.; Tian, J. H.; Pei, Y. Y.; Yuan, M. L.; Zhang, Y. L.; Dai, F. H.; Liu, Y.; Wang, Q. M.; Zheng, J. J.; Xu, L.; Holmes, E. C.; Zhang, Y. Z. A New Coronavirus Associated with Human Respiratory Disease in China. *Nature* **2020**, *579* (7798), 265−269.

(3) Zhou, P.; Yang, X.-L.; Wang, X. G.; Hu, B.; Zhang, L.; Zhang, W.; Si, H. R.; Zhu, Y.; Li, B.; Huang, C. L.; Chen, H. D.; Chen, J.; Luo, Y.; Guo, H.; Jiang, R. Di; Liu, M. Q.; Chen, Y.; Shen, X. R.; Wang, X.; Zheng, X. S.; Zhao, K.; Chen, Q. J.; Deng, F.; Liu, L. L.; Yan, B.; Zhan, F. X.; Wang, Y. Y.; Xiao, G. F.; Shi, Z. L. A Pneumonia Outbreak Associated with a New Coronavirus of Probable Bat Origin. *Nature* **2020**, *579* (7798), 270−273.

(4) Anfinrud, P.; Stadnytskyi, V.; Bax, C. E.; Bax, A. Visualizing Speech-Generated Oral Fluid Droplets with Laser Light Scattering. *N. Engl. J. Med.* **2020**, *382* (21), 2061−2062.

(5) Setti, L.; Passarini, F.; De Gennaro, G.; Barbieri, P.; Perrone, M. G.; Borelli, M.; Palmisani, J.; Di Gilio, A.; Piscitelli, P.; Miani, A. Airborne Transmission Route of Covid-19: Why 2 Meters/6 Feet of Inter-Personal Distance Could Not Be Enough. *Int. J. Environ. Res. Public Health* **2020**, *17* (8), 2932.

(6) Jones, N. R.; Qureshi, Z. U.; Temple, R. J.; Larwood, J. P. J.; Greenhalgh, T.; Bourouiba, L. Two Metres or One: What Is the Evidence for Physical Distancing in Covid-19? *BMJ.* **2020**, *370*, m3223.

(7) Liao, L.; Xiao, W.; Zhao, M.; Yu, X.; Wang, H.; Wang, Q.; Chu, S.; Cui, Y. Can N95 Respirators Be Reused after Disinfection? How Many Times? *ACS Nano* **2020**, *14* (5), 6348−6356.

(8) Zhao, M.; Liao, L.; Xiao, W.; Yu, X.; Wang, H.; Wang, Q.; Lin, Y. L.; Kilinc-Balci, F. S.; Price, A.; Chu, L.; Chu, M. C.; Chu, S.; Cui, Y. Household Materials Selection for Homemade Cloth Face Coverings and Their Filtration Efficiency Enhancement with Triboelectric Charging. *Nano Lett.* **2020**, *20* (7), 5544−5552.

(9) Lustig, S. R.; Biswakarma, J. J. H.; Rana, D.; Tilford, S. H.; Hu, W.; Su, M.; Rosenblatt, M. S. Effectiveness of Common Fabrics to Block Aqueous Aerosols of Virus-like Nanoparticles. *ACS Nano* **2020**, *14* (6), 7651−7658.

(10) Konda, A.; Prakash, A.; Moss, G. A.; Schmoldt, M.; Grant, G. D.; Guha, S. Aerosol Filtration Efficiency of Common Fabrics Used in Respiratory Cloth Masks. *ACS Nano* **2020**, *14* (5), 6339−6347.

(11) Shrestha, A.; Mahmood, A. Review of Deep Learning Algorithms and Architectures. *IEEE Access* **2019**, *7*, 53040−53065.

(12) Lecun, Y.; Bengio, Y.; Hinton, G. Deep Learning. *Nature* **2015**, *521* (7553), 436−444.

(13) Sommer, C.; Straehle, C.; Kothe, U.; Hamprecht, F. A. Ilastik: Interactive Learning and Segmentation Toolkit. *Proc. - Int. Symp. Biomed. Imaging* **2011**, *2014*, 230−233.

(14) Ronneberger, O.; Fischer, P.; Brox, T. U-Net: Convolutional Networks for Biomedical Image Segmentation. In *Medical Image Computing and Computer-Assisted Intervention - MICCAI 2015*; MICCAI 2015. Lecture Notes in Computer Science, vol *9351*; Navab, N., Hornegger, J., Wells, W., Frangi, A., Eds.; Springer: Switzerland, 2015; pp 234−241 DOI: 10.1007/978-3-319-24574-4_28.

(15) Falk, T.; Mai, D.; Bensch, R.; Cicek, O.; Abdulkadir, A.; Marrakchi, Y.; Bohm, A.; Deubner, J.; Jackel, Z.; Seiwald, K.; Dovzhenko, A.; Tietz, O.; Dal Bosco, C.; Walsh, S.; Saltukoglu, D.; Tay, T. L.; Prinz, M.; Palme, K.; Simons, M.; Diester, I.; Brox, T.; Ronneberger, O. U-Net: Deep Learning for Cell Counting, Detection, and Morphometry. *Nat. Methods* **2019**, *16* (1), 67−70.

(16) Smistad, E.; Falch, T. L.; Bozorgi, M.; Elster, A. C.; Lindseth, F. Medical Image Segmentation on GPUs - A Comprehensive Review. *Med. Image Anal.* **2015**, *20* (1), 1−18.

(17) Lee, Y.; Wadsworth, L. C. Structure and Filtration Properties of Melt Blown Polypropylene Webs. *Polym. Eng. Sci.* **1990**, *30* (22), 1413−1419.

(18) De Rovere, A.; Shambaugh, R. L.; O'Rear, E. Investigation of Gravity-Spun, Melt-Spun, and Melt-Blown Polypropylene Fibers Using Atomic Force Microscopy. *J. Appl. Polym. Sci.* **2000**, *77*, 1921−1937.

(19) Nayak, R.; Kyratzis, I. L.; Truong, Y. B.; Padhye, R.; Arnold, L.; Peeters, G.; O'Shea, M.; Nichols, L. Fabrication and Characterisation of Polypropylene Nanofibres by Meltblowing Process Using Different Fluids. *J. Mater. Sci.* **2013**, *48* (1), 273−281.

(20) Chang, J. S.; Lawless, P. A.; Yamamoto, T. Corona Discharge Processes. *IEEE Trans. Plasma Sci.* **1991**, *19* (6), 1152−1166.

(21) Overney, R. M.; Lüthi, R.; Haefke, H.; Frommer, J.; Meyer, E.; Güntherodt, H. J.; Hild, S.; Fuhrmann, J. An Atomic Force Microscopy Study of Corona-Treated Polypropylene Films. *Appl. Surf. Sci.* **1993**, *64* (3), 197−203.

(22) Kravtsov, A.; Brünig, H.; Zhandarov, S.; Beyreuther, R. Electret Effect in Polypropylene Fibers Treated in a Corona Discharge. *Adv. Polym. Technol.* **2000**, *19* (4), 312−316.

(23) Yovcheva, T. A.; Avramova, I. A.; Mekishev, G. A.; Marinova, T. S. Corona-Charged Polypropylene Electrets Analyzed by XPS. *J. Electrost.* **2007**, *65* (10−11), 667−671.

(24) Ragoubi, M.; George, B.; Molina, S.; Bienaimé, D.; Merlin, A.; Hiver, J. M.; Dahoun, A. Effect of Corona Discharge Treatment on Mechanical and Thermal Properties of Composites Based on Miscanthus Fibres and Polylactic Acid or Polypropylene Matrix. *Composites, Part A* **2012**, *43* (4), 675−685.

(25) Schneider, C. A.; Rasband, W. S.; Eliceiri, K. W. NIH Image to ImageJ: 25 Years of Image Analysis. *Nat. Methods* **2012**, *9* (7), 671−675.

(26) Makovetsky, R.; Piche, N.; Marsh, M. Dragonfly as a Platform for Easy Image-Based Deep Learning Applications. *Microsc. Microanal.* **2018**, *24* (S1), 532−533.

(27) Badran, A.; Marshall, D.; Legault, Z.; Makovetsky, R.; Provencher, B.; Piché, N.; Marsh, M. Automated Segmentation of Computed Tomography Images of Fiber-Reinforced Composites by Deep Learning. *J. Mater. Sci.* **2020**, *55* (34), 16273−16289.

■ NOTE ADDED AFTER ASAP PUBLICATION

Due to a production error, this paper was published ASAP on December, 7, 2020, with missing information from the Associated Content section. The corrected version was reposted on December 7, 2020.